# Automatic Two-Step Detection of Pulmonary Nodules

Martin Dolejší, Jan Kybic

Faculty of Electrical Engineering, Czech Technical University in Prague, Czech Republic

## ABSTRACT

We present a computer-aided diagnosis (CAD) system to detect small-size (from 2mm to around 10mm) pulmonary nodules from helical CT scans. A pulmonary nodule is a small, round (parenchymal nodule) or worm (juxta-pleural) shaped lesion in the lungs. Both have greater radio density than lungs parenchyma. Lung nodules may indicate a lung cancer and its detection in early stage improves survival rate of patients. CT is considered to be the most accurate imaging modality for detection of nodules. However, the large amount of data per examination makes the interpretation difficult. This leads to omission of nodules by human radiologist. CAD system presented is designed to help lower the number of omissions. Our system uses two different schemes to locate juxtapleural nodules and parenchymal nodules. For juxtapleural nodules, morphological closing and thresholding is used to find nodule candidates. To locate non-pleural nodule candidates, 3D blob detector uses multiscale filtration. Ellipsoid model is fitted on nodules. To define which of the nodule candidates are in fact nodules, an additional classification step is applied. Linear and multi-threshold classifiers are used. System was tested on 18 cases (4853 slices) with total sensitivity of 96%, with about 12 false positives/slice. The classification step reduces number of false positives to 9 per slice without significantly decreasing sensitivity (89,6%).

**Keywords:** computer aided diagnostic, nodule detection, BW morphology, 3D filtering, ellipsoid fitting, pattern recognition.

## 1. INTRODUCTION

Lung cancer is one of the leading causes of death in USA[9] and civilized world. Surgery, radiation therapy, and chemotherapy are used in the treatment of lung carcinoma. In spite of that, the five-year survival rate for all stages combined is only 14%. However, early detection helps significantly—it is reported[10] that the survival rate for early-stage localized cancer (stage I) is 49%.

CT is considered to be the most accurate imaging modality available for early detection and diagnosis of lung cancer. It allows detecting pathological deposits as small as 1mm in diameter. These deposits are called lung nodules.

However, the large amount of data per examination makes the interpretation tedious and difficult, leading to a high false-negative rate for detecting small nodules. Suboptimal acquisition parameters (e.g. pitch) further decrease the detection rate. A simulation study demonstrated[1] the overall detection rate to be only 63% for nodules of 1–7 mm in diameter. As the size of the nodule decreased, the sensitivity fell to 1% for nodules smaller than 1.5mm. Retrospective analysis of CT scans often shows undetected nodules on the initial scans of oncological patients.[2]

Image processing and visualization techniques for volumetric CT data sets may improve the radiologist's ability to detect small lung nodules. For example, reconstruction of CT images with narrow interscan spacing[3] and interpretation of images using cine rather than film-based viewing technique,[4] have been reported to improve small nodule detection.

There are many projects in CT image processing dealing with nodule detection. They can be divided into two groups of approaches: density-based and model-based approaches. Density-based detection methods employ techniques such as multiple thresholding,[11] region-growing,[12] locally adaptive thresholding in combination with region-growing[13] and fuzzy clustering[14] to identify nodule candidates in the lungs. For the model-based detection approaches, the relatively compact shape of a small lung nodule is taken into account while establishing

---

e-mail: dolejm1@fel.cvut.cz

the models to identify nodules in the lungs. Techniques such as "N-Quoit filter"[15] template-matching,[16] object-based deformation[17] and the anatomy-based generic model[18] have been proposed to identify sphere-shaped small nodules in the lungs. Other attempts include automated detection of lung nodules by analysis of curved surface morphology[19] and improvement of the nodule detection by subtracting broncho-vascular structures from the lung images.[20]
This work is based on our earlier approach.[25]

## 1.1. Nodules

A solitary pulmonary nodule[22] (parenchymal, non-pleural nodule) is a small, round or egg-shaped lesion in the lungs. Juxtapleural pulmonary nodule is a small, worm-shaped lesion connected to pleura. (Figure 1)

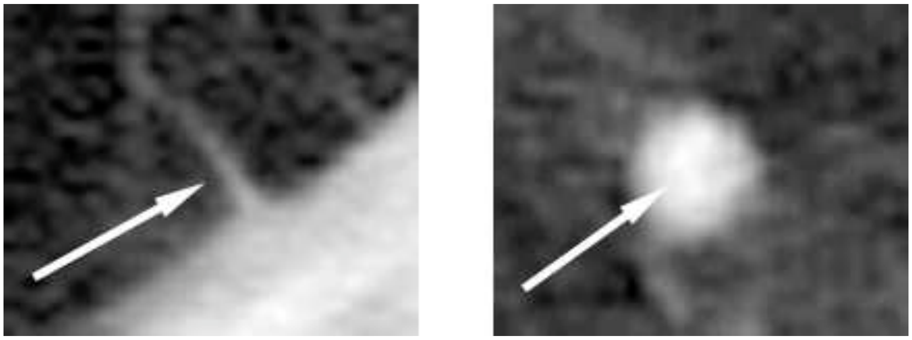

**Figure 1.** Nodule examples: juxtapleural nodule (left), parenchymal nodule (right).

Nodules are typically asymptomatic, and they are usually noticed by chance on a chest X-ray that has been done for another reason. They are usually smaller than 3–4 cm in diameter (no larger than 6 cm) and are always surrounded by normal, functioning lung tissue. Their intensity in CT scans is from -300 to 0 HU.

# 2. METHODS

Our fully automatic nodule candidate detection algorithm uses thresholding-based segmentation, blob detector using multiscale LoG filters with post processing for parenchymal nodule candidates detection, and mathematical morphology tools for juxtapleural nodule candidates detection. Next step consists of applying an automatic nodule classification system based on geometrical and image features to the candidates. We have tested a linear classifier and a classifier based on thresholding.

## 2.1. Lungs Segmentation

Lungs can be easily separated from other anatomic structures by binary thresholding at -350HU (Figure 4a)

$$m_1(x,y,z) = Thr\big(f(x,y,z); -350HU\big).$$

On Figure 2 you can see lighter tissue (fat and muscle) around the lungs used for segmentation, on Figure 3 is a histogram of the same image.

After thresholding, the background (the outside of the body) is eliminated by suppressing all components adjacent to image edges by flood-filling. This gives us a lung mask $m(x,y,z)$ (1 as lungs, 0 background) (Figure 4b)

## 2.2. Nodule Candidates Finding

Both types of nodules, juxtapleural and parenchymal, are high density objects (in CT images appear as bright). Because of a big difference in shape, we have decided to perform detection of these two classes independently.

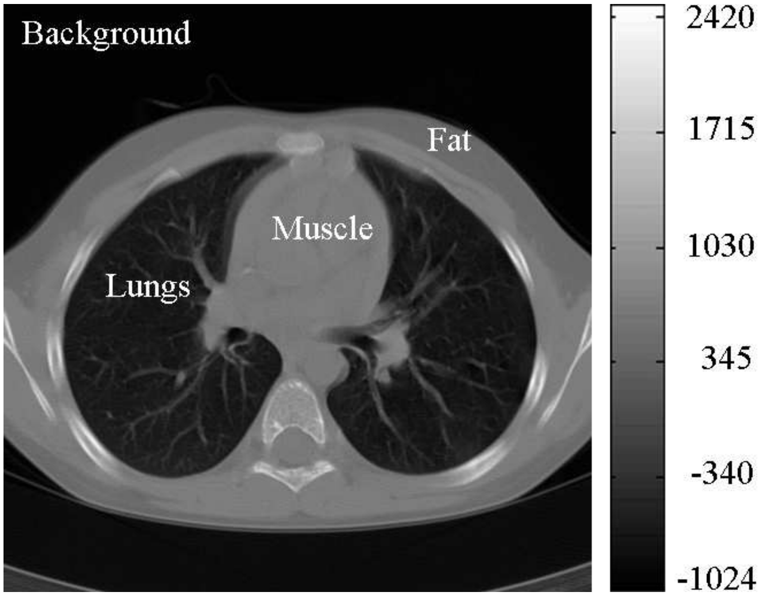

**Figure 2.** Original CT slice and tissues localization. Intensity values are given in HU.

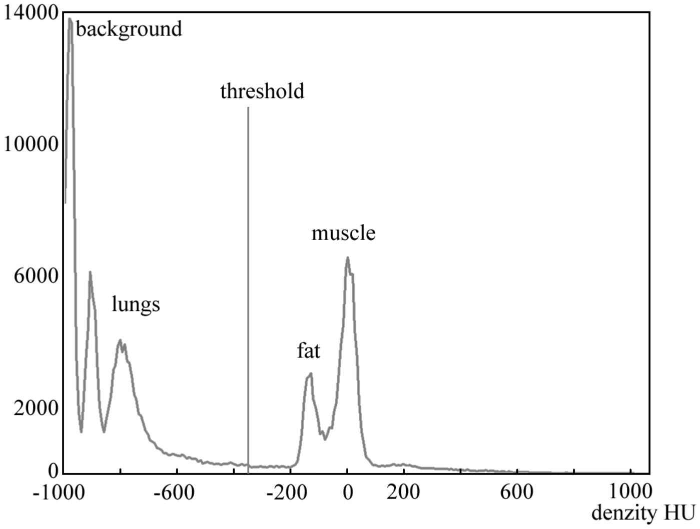

**Figure 3.** Histogram of the image in Figure 2 and the segmentation threshold (red).

## 2.3. Parenchymal Nodules

Input of a parenchymal nodule detector is a 3D image $f(x, y, z)$ and the lung mask $m(x, y, z)$ from segmentation. For better results the lung mask is smoothed (Figure 4c) by morphological closing with spherical element $e(x, y, z)$ with 9mm in diameter. The smoothed mask is then:

$$s(x, y, z) = m(x, y, z) \bullet e(x, y, z)$$

Image $f(x, y, z)$ is multiplied by the smoothed mask $s(x, y, z)$ element by element

$$g(x, y, z) = f(x, y, z) \cdot s(x, y, z).$$

From the segmented lungs image a nodule candidates are detected by a multiscale 3D blob detector.

Blob detector[6] is a filtration algorithm which is used for detection of spherical object in images. One of the first, and also the most common blob detector is based on the LoG filter. Input image $f(x,y,z)$ filtered by LoG filters with diameter $d_k$=5.5, 8, 10, and 12.5mm. These diameters cover the range of typical dimensions of nodules. The relationship between diameter $d_k$ and variance $\sigma_k$ of each filter[23] is

$$\sigma_k^2 = \left(\frac{d_k - 1}{3}\right)^2 .$$

In filtered images $s_k(x,y,z) = f(x,y,z) * l_{\sigma_k}(x,y,z),\ k = 1 \ldots 4$, local maximas $m_k(x,y,z)$ are found. Pixels with value greater than all pixels in they 26-neighborhood $n_{26}(x,y,z)$ are set to 1. Every other pixel is set to 0.

Local maximum is than traced from the finest scale image $m_1(x,y,z)$ to the coarest scale image $m_4(x,y,z)$ by morphological dilatating and multiplication. For example, $m_1(x,y,z)$ is dilatated by a quantized elipsoid

$$e(x,y,z) = \left\{ (x,y,z); |z| \leq 1 \wedge x^2 + y^2 \leq \left\{ \begin{array}{ll} 9; & z = 0 \\ 2; & |z|<1 \end{array} \right. \right\}$$

and multiplied element-wise with $m_2(x,y,z)$

$$m_1'(x,y,z) = \big(m_1(x,y,z) \oplus e(x,y,z)\big) \cdot m_2(x,y,z).$$

I other words, if some maxima from $m_2(x,y,z)$ is in the $e(x,y,z)$-neighbourhood of points from $m_1(x,y,z)$, is saved to the next step, every other maxima thrown away.

As result, in $m_{x4}(x,y,z)$ we have stable maximas, which do not significantly change position between scales. These points are interpreted as potential parenchymal nodule centers.

**Figure 4.** Progress of lung mask generation: (a) thresholding, (b) flood filling, (c) smoothing.

## 2.4. Juxtapleural Nodules

This part of the detector works on each slice separately, because of almost no regularity of the juxta-pleural nodules in the z-direction.

The detector operates on the smoothed mask $s(x,y,z)$ and the original image $f(x,y,z)$ thresholded at -600HU. High density nodules appear as one-valued (white) irregularities on the lung edges (Figure 5a) after thresholding, so subtraction of the thresholded image $t(x,y,z)$ and the smoothed mask $s(x,y,z)$ shows them well

$$j_0(x,y,z) = s(x,y,z) - t(x,y,z).$$

In the next step objects not located on lung boundary are eliminated from $j_0(x,y,z)$ by the following procedure. Lungs boundary is generated from the smoothed mask by morphological eroding and subtracting

$$b(x,y,z) = s(x,y,z) - \big(s(x,y,z) \ominus e_1(x,y,z)\big),$$

where $e_1$ is disc element of 2.5mm in diameter (Figure 5b). The mask $j_0(x,y,z)$ is then multiplied element by element by boundary mask $b(x,y,z)$

$$j(x,y,z) = g(x,y,z) \cdot b(x,y,z).$$

Finally, large objects (greater than 29mm$^2$) in each slice are eliminated because of small expected dimensions of juxtapleural nodules (Figure 5c).

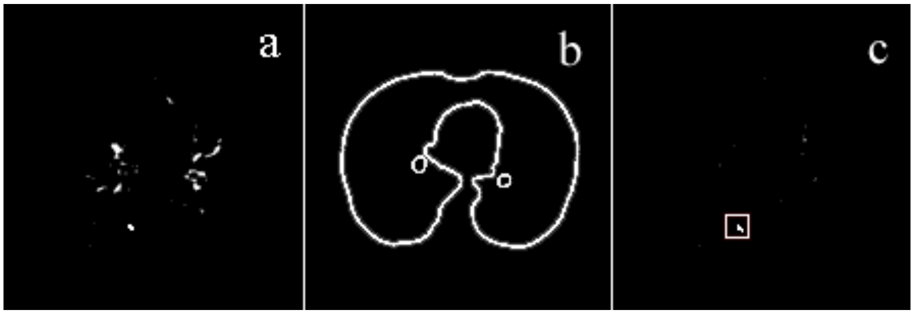

**Figure 5.** Juxtapleural nodule detection: (a) mask $j_0(x,y,z)$, (b) lung edge $b(x,y,z)$ (c) small object on an edge.

## 2.5. Nodule Candidates Clasification

Classification divides candidate points from parenchymal ($\mathbf{p} = (p_x, p_y, p_z) \in P$) and juxta-pleural ($\mathbf{j} = (j_x, j_y, j_z) \in J$) detectors to two classes: nodule and non-nodule. Ideally, the classifier should correctly detect all true nodules, and also correctly reject all non-nodules. This leads to a decrease of the number of FP results with constant number of TPs.

### 2.5.1. The Geometrical Model

Points from detectors (Sections 2.3 and 2.4) are described by their centers $\mathbf{p}$ and $\mathbf{j}$. For successful classification, more descriptors (features) than only a center are needed. We will classify each nodule candidate according to its shape. To describe nodules we choose an ellipsoid model

$$E = \left\{ f(x,y,z) : \frac{(x-x_0)^2}{a^2} + \frac{(y-y_0)^2}{b^2} + \frac{(z-z_0)^2}{c^2} \leq 1; \mathbf{x} = (x_0, y_0, z_0) \in X \right\}.$$

further rotated by angles $\varphi$ and $\vartheta$ around coordinate axes.

Parameters of the ellipsoid model $E$ are $a, b, c, \varphi, \vartheta$, and we will consider them as a vector $\mathbf{s} = (a, b, c, \varphi, \vartheta)$. The center $(x_0, y_0, z_0)$ of the ellipsoid $E$ is optimized independently (see next Section).

### 2.5.2. Exact Center Specification

First we find the center $(x_0, y_0, z_0)$ of the future ellipsoid. We need to do it, because the nodule candidate center $(x_c, y_c, z_c)$ obtained either from parenchymal or juxtapleural nodule candidates detectors is normally not accurate enough.

We proceed as follows: We take a cube neighborhood

$$c_1(x_c, y_c, z_c) = \{(x,y,z) : x - x_c + y - y_c + z - z_c \leq 7mm\}$$

of each $\mathbf{x} \in X$ and threshold it at -720HU

$$o(x,y,z) = T_{hr}\big(f(x,y,z); -750HU\big), (x,y,z) \in c_1.$$

The nearest object in the sense of Euclidean distance (pixel of value 1) to $\mathbf{x}$ in $o(x,y,z)$ is found. All other objects (not connected to nearest one) are eliminated from $o(x,y,z)$. Center of the single object now present in $o(x,y,z)$ is localized by repeatable morphological erosion by 3D structural element created as 6-neighbourhood of center pixel, until the object disappears.

We take the improved center $\mathbf{x}$ from last nonempty erosion step, as its center of mass. Number of erosions is a first estimation $(a, b, c)$ of the radius of the ellipsoid.

### 2.5.3. Intensity Threshold Finding

Once the center $\mathbf{x}$ is known, we need to find a threshold $T$. We define a new cubical neighbourhood

$$c_2(x_0, y_0, z_0) = \{(x, y, z) : x - x_0 + y - y_0 + z - z_0 \leq r + 6\text{pixels}\}$$

and cut it along coordinate axes (Figure 6 top) as follows: $f_x(x) = f(x, 0, 0),\ f_y(y) = f(0, y, 0),\ f_z(z) = f(0, 0, z)$ and find the positions of the maximum and minimum derivatives along each cut $\mathrm{g}\big(f_x(x)\big) = \frac{\mathrm{d}f_x}{\mathrm{d}x}$, $\mathrm{g}\big(f_y(y)\big) = \frac{\mathrm{d}f_y}{\mathrm{d}y}$, $\mathrm{g}\big(f_z(z)\big) = \frac{\mathrm{d}f_z}{\mathrm{d}z}$ (Figure 6 bottom). The threshold $T$ is computed as the mean intensity of voxels at the positions of the maximum derivatives

$$T = \frac{I_{x+} + I_{x-} + I_{y+} + I_{y-} + I_{z+} + I_{z-}}{6}.$$

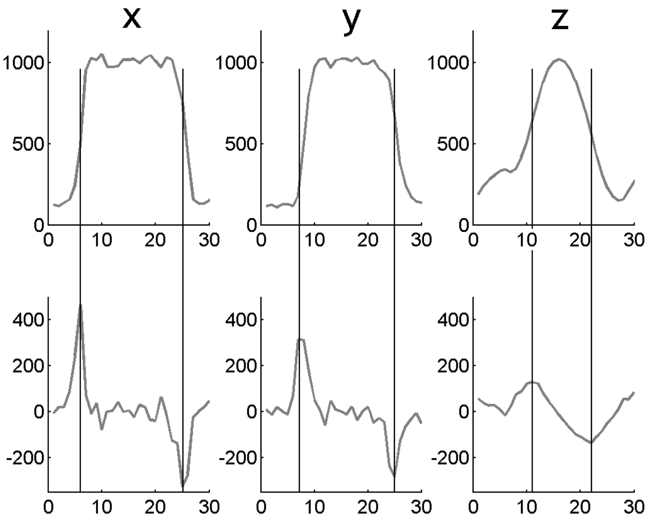

**Figure 6.** Intensity profiles $f_x(x)$, $f_y(y)$, $f_z(z)$ of nodule along coordinate axes (top) and correspondent gradients (bottom)

### 2.5.4. Ellipsoid Parameters Ftting

The parameters $\mathbf{s} = (a, b, c, \varphi, \vartheta)$ of the ellipsoid are found by maximization of a criterion

$$J(\mathbf{s}) = \sum_{(x,y,z)\in E} f(x, y, z) - T. \tag{1}$$

By maximizing $J$ we are looking for ellipsoid which contains as many pixels as possible with intensity greater than $T$, and every pixel with intensity less than T in ellipsoid is penalized. An initial guess is $a, b, c = r + 3,\ \varphi = 0,\ \vartheta = 0$. Examples of fitted ellipsoids are in Figure 7.

## 3. CLASSIFICATION

Classifier[8] is a device with $n$ inputs and one output. Inputs are represented by an input vector $\mathbf{x} = (x_1, \ldots, x_i)$. We are using a 2-class classifier with output $y \in \{\text{'nodule'}, \text{'not nodule'}\}$.

The function $d(\mathbf{x}) = y$ is called a decision rule. The form of the rule is given by classifier design, its parameters by a learning process. The input to the learning process is a set $T = \big\{(x_1, y_1), \ldots, (x_l, y_l)\big\}$ of binary labeled $y_i \in \{1, 2\}$ training vectors $\mathbf{x}_i \in \mathbb{R}^n$. Let $I_y = \{i : y_i = y\}, y \in \{1, 2\}$ be sets of indices of the training vectors belonging to the first $(y = 1)$ and the second class $(y = 2)$.

### 3.1. Classifiers

Two classifiers were tested. First, a simple multi-threshold clasifier. Second, a linear classifier based on Fisher linear discriminant.[21] For both classifiers the same eight input shape descriptors of each nodule are used[24]:

$$\begin{array}{llcl}
\text{effective radius} & d_1 & = & \sqrt[3]{abc} \\
\text{discircularity} & d_2 & = & \max(a,b,c) - r_{ef} \\
\text{elongation} & d_3 & = & \frac{\max(a,b,c)}{\min(a,b,c)} \\
\text{mean intensity} & d_4 & = & \sum_{(x,y,z)\in E} f(x)/\text{number of pixels} \in E \\
\text{intensity sum} & d_5 & = & \sum_{(x,y,z)\in E} f(x) \\
\text{number of pixels} & d_6 & = & \text{number of pixels} \in E \\
\text{variance of intensity} & d_7 & = & \operatorname{var}\big(\{f(x,y,z) : (x,y,z) \in E\}\big) \\
\text{threshold} & d_8 & = & \text{the intensity threshold } T
\end{array}$$

Input data for classifiers learning are acquired by an ellipsoid fitting procedure.

#### 3.1.1. Fisher Linear Discriminant

Classifier based on FLD[21] uses one linear discrimination function

$$g(\mathbf{x}) = b + q_1 d_n + \ldots, q_n d_n.$$

This classifier maximizes the class separability. The class separability in a direction $\mathbf{q} \in \mathbb{R}^n$ is defined as

$$F(\mathbf{q}) = \frac{\langle \mathbf{q} \cdot \mathbf{S_B q} \rangle}{\langle \mathbf{q} \cdot \mathbf{S_Q q} \rangle}, \tag{2}$$

where $\mathbf{S_B}$ is the between-class scatter matrix

$$\mathbf{S_B} = (\boldsymbol{\mu}_1 - \boldsymbol{\mu}_2)(\boldsymbol{\mu}_1 - \boldsymbol{\mu}_2)^T, \quad \boldsymbol{\mu}_y = \tfrac{1}{|I_y|} \textstyle\sum_{i \in I_y} \boldsymbol{d}_i, y \in \{1,2\},$$

and $\boldsymbol{S_Q}$ is the within class scatter matrix defined as

$$\mathbf{S_Q} = \boldsymbol{S}_1 + \boldsymbol{S}_2, \quad \mathbf{S}_y = \textstyle\sum_{i \in Y_y} (\boldsymbol{d}_i - \boldsymbol{\mu}_y)(\boldsymbol{d}_i - \boldsymbol{\mu}_y)^T, y \in \{1,2\}.$$

In the case of the FLD, the parameter vector $\mathbf{q}$ of the linear discriminant function $g(d) = \langle \boldsymbol{q} \cdot \boldsymbol{x} \rangle + b$ is determined to maximize the class separability criterion (2)

$$\boldsymbol{q} = \arg\max_{\boldsymbol{q}'} F(\boldsymbol{q}'). \tag{3}$$

Which is equivalent to a generalized eigen-value problem[7]

$$\mathbf{S_B q} = \lambda \mathbf{S_Q q}.$$

The problem (3) can be solved by the matrix inversion

$$\boldsymbol{q} = \boldsymbol{S_Q}^{-1}(\boldsymbol{\mu}_1 - \boldsymbol{\mu}_2).$$

The bias $b$ of the linear rule must be determined based on another principle, by solving equality

$$\langle \boldsymbol{q} \cdot \mu_1 \rangle + b = -\big(\langle \boldsymbol{q} \cdot \mu_2 \rangle + b\big),$$

since we consider the same distance of $b$ from each class.

### 3.1.2. Multiple Thresholding

A very simple nonlinear classifier is based on multiple thresholding. The decision rule uses $2n$ thresholds where $n$ is number of descriptors.

If all elements of input vector are between corresponding thresholds, vector is classified as 'nodule', if not, as 'not nodule'

$$y = \begin{cases} \text{'nodule'} & \forall k \in \{1, \dots 8\};\ l_k \leq x_k \leq h_k \\ \text{'not nodule'} & \text{otherwise,} \end{cases}$$

where $l_k,\ h_k$ are low and high thresholds.

Learning consists of searching the biggest and the smallest value of each parameter in $P_y = \{\boldsymbol{x}_i : y_i = 1\}$ from the training set.

## 4. RESULTS

### 4.1. Test Data

Our test data consist of 18 CT volume scans (18 patients, 4853 slices) for which ground truth nodule information was available. In total, there were 222 known nodules, 74 juxtapleural and 148 parenchymal. All data was acquired on Somatom AR Star CT machine (Siemens). Resolution of images was 1.6pixels per mm.

### 4.2. Evaluation Criteria for Detector Performance

Our detector (see Sections 2.3 and 2.4) and classifiers (Section 2.5) provide for each detected nodule the coordinates of its center $\mathbf{x} = (x, y, z)$. If the distance between the detected point $\mathbf{x} = (x, y, z)$ and closest ground truth point $\mathbf{g} = (x, y, z)$ is smaller than 3mm

$$|\mathbf{x} - \mathbf{g}| \leq 3mm,$$

nodule is considered as correctly detected and counted as a true positive result (TP). Every other detected point is considered as false positive (FP). If there is no point detected in a 3mm neighbourhood of the ground truth, the point is considered as false negative (FN). We also define true negative results (TN) as FP points detected by nodule candidates detectors and classified to class 'not nodule' by a classifier.
We have calculated the following statistics:

**FPs/slice:** the average number of FPs per slice

**Sensitivity:** Number of detected nodules to total number of nodules present

$$\text{sensitivity} = \frac{\text{TPs}}{\text{TPs+FPs}}$$

**Specificity:** Number of TNs to total number of not detected nodules

$$\text{specificity} = \frac{\text{TNs}}{\text{FPs+TNs}}$$

### 4.3. Algorithm Performance

Nodule candidate detectors works each with sensitivity about 96%. The number of FPs is 12 FPs/slice, 6 from juxta-pleural, 6 from parenchymal detector, see Tables 1 and 4. This justifies our decision of further classification step to decrease the number of FPs.

Classifiers learned by the leave-one out method were then tested on nodule candidates. Results are in Table 4. Confusion matrices for FLD based and multi-threshold classifiers are in Tables 2 and 3. We show some detection results in Figures 7–11.

The algorithm was implemented in Matlab. The processing of one examination takes about six hours. Detection only (fitting and classification) takes about one and half hours.

| | |
|---|---|
| TP= 213 | FN= 9 |
| FP= 58359 | TN= — |

**Table 1.** Confusion matrix of nodule candidate detection

| | |
|---|---|
| TP= 165 | FN= 57 |
| FP= 12704 | TN= 45655 |

**Table 2.** Confusion matrix of FLD classifier.

## 5. CONCLUSIONS

We have developed an automatic method for nodule detection. We are using a two step approach: ROI detection and classification. The method was validated on data with 222 real nodules.

Our system performance can be adjusted between total sensitivity 95,9% with 12FPs/slice (when no classifier used) and total sensitivity 74,3% with 2.6FPs/slice (when FLD based classifier applied). See Table 4.

We observed some nodule-like objects in testing data detected by algorithm and not included in ground truth information. These might be nodules missed by the human expert.

### Acknowledgements

The CT data were provided by a Faculty Hospital, Motol, Prague.

This work was supported by the Czech Ministry of Health under project NR8314-3/2005, and by the Grant Agency of the Czech Academy of Sciences under Project 1ET101050403.

## REFERENCES

1. D. P. Naidich, H. Rusinek, G. McGuinness, B. Leitman, D. I. McCauley, C. I. Henschke. *Variables affecting pulmonary nodule detection with computed tomography: evaluation with three-dimensional computer simulation.* J. Thorac Imaging no. 8.
2. J. W. Gurney: *Missed lung cancer at CT. imaging findings in nine patients* Radiology no. 199, 1996.
3. J. A. Buckley, W. W. Scott, S. S. Siegelman, J. E. Kuhlman, B. A. Urban, D. A. Bluemke, E. K. fishman *Pulmonary nodules: Effect of increased data sampling on detection with spiral CT and confidence in diagnosis.* Radiology no. 196, 1995.
4. S. E. Seltzer, P. F. Judy, D. F. Adams, F. L. Jacobson, P. Stark, R. Kikinis, R. G. Swensson, S. Hooton, B. Head, U. Feldman. *Spiral CT of the chest: comparison of cine and film-based viewing.* Radiology no. 197, 1995.
5. B. van Ginneken, T. H. Romeny, M. A. Viergever. *Computer-Aided Diagnosis in Chest Radiography: A Survey.* IEEE Transactions on medical imaging, vol. 20, no. 12, 2001.
6. T. Lindeberg. *Feature Detection with Automatic Scale Selection.* J. of Computer Vision, vol. 30, no. 2, 1998.
7. R. O. Duda, P. E. Hart, D. G. Stork. *Pattern Classification.* John Wiley & Sons, 2nd. edition, 2001. Chapter 3
8. M. Sonka, V. Hlavac, R. Boyle. *Image Processing, Analysis, and Machine Vision.* PWS Publishing, 2nd. edition, 1998. ISBN 0-534-95393-X
9. American Cancer Society. *ACS cancer facts and figures 2002.* American Cancer Society, Atlanta, GA, 2003.
10. L. Ries et al. *SEER Cancer Statistics Review 1973–1996.* National Cancer Institution, Bethesda, MD, 1999.
11. J. P. Ko, M. Betke. *Chest CT: Automated Nodule Detection and Assessment of Change Over Time-Preliminary experience.* Radiology 218, 2001, pp. 267–273.
12. M. Fiebich, C. Wietholt, B. C. Renger, S. Armato, K. Hoffmann, D. Wormanns, S. Diederich. *Automatic detection of pulmonary nodules in low-dose screening thoracic CT examinations.* Proc. SPIE, vol. 3661, 1999, pp. 1434–1439.
13. L. Fan, C. L. Novak, J. Qian, G. Kohl, D. P. Naidich. *Automatic detection of lung nodules from multi-slice low-dose CT images.* Proc. SPIE, vol. 4322, 2001, pp. 1828–1835.

| | |
|---|---|
| TP= 199 | FN= 23 |
| FP= 43652 | TN= 17707 |

**Table 3.** Confusion matrix of multi-threshold classifier.

| | **Sensitivity [%]** | **Specificity [%]** | **FP/slice** |
|---|---:|---:|---:|
| **Detection** | 95.9 | — | 12.0 |
| **FLD class.** | 74.3 | 78.2 | 2.6 |
| **Thr. class.** | 89.6 | 25.2 | 9.0 |

**Table 4.** Experimental results of algorithm

14. H. Satoh, Y. Ukai, N. Niki, K. Eguchi, K. Mori, H. Ohmatsu, R. Kakinuma, M. Kaneko, N. Moriyama. *Computer aided diagnosis system for lung cancer based on retrospective helical CT images* Proc. SPIE, vol. 3661, 1999, pp. 1324–1335.
15. T. Okumura, T. Miwa, J. Kako, S. Yamamoto, M. Matsumoto, Y. Tateno, T. Linuma, T. Matsumoto. *Image processing for computer-aided diagnosis of lung cancer screening system by CT (LSCT).* Proc. SPIE, vol. 3338, 1998, pp. 1314–1322.
16. Y. Lee, T. Hara, H. Fujita, S. Itoh, T. Ishigaki. *Automated detection of pulmonary nodules in helical CT images based on an improved template matching technique.* IEEE Transaction on Medical Imaging, vol.20, 2001, pp. 595–604.
17. S. Lou, C. Chang, K. Lin, T. Chen. *Object-Based Deformation Technique for 3-D CT Lung Nodule Detection.* Proc. SPIE, vol. 3661, 1999, pp. 1544–1552.
18. M. S. Brown, M. F. McNitt-Gray, J. G. Goldin, R. D. Suh, J. W. Sayre, D. R. Aberle. *Patient-specific models for lung nodule detection and surveillance in CT images.* IEEE Transaction on Medical Imaging, vol.20, 2001, pp. 1242–1250.
19. H. Taguchi, Y. Kawata, N. Niki, H. Satoh, H. Ohmatsu, R. Kakinuma, K. Eguchi, M. Kaneko, N. Moriyama. *Lung cancer detection based on helical CT images using curved surface morphology analysis.* Proc. SPIE, vol. 3661, 1999, pp. 1307–1314.
20. P. Croisille, M. Souto, M. Cova, S. Wood, Y. Afework, J. Kuhlman, E. Zerhouni. *Pulmonary nodules: improved detection with vascular segmentation and extraction with spiral CT.* Radiology, vol. 197, 1995, pp. 397–401.
21. V. Franc, V. Hlavac. *Statistical Pattern Recognition Toolbox for Matlab, Users guide.* June 24, 2004, available at ftp://cmp.felk.cvut.cz/pub/cmp/articles/Franc-TR-2004-08.pdf
22. The Pulmonology Cannel. *Solitary Pulmonary Nodule: Overview.* [online] [cit. 20.12.2006], available at http://www.pulmonologychannel.com/spn/
23. B. Sümengen *Blob detector.* available at http://barissumengen.com/myblog/index.php?id=3
24. J. Beutel, H. L. Kandel, R. L. Van Mettel. *Handbook of Medical Imaging, Volume 2. Medical Image Processing and Analysis.* SPIE Press, 2000 , ISBN 0-8194-3622-4.
25. M. Dolejší, J. Kybic. *Detection of Pulmonary Nodules in CT Scans.* Proc. Biosignál 2006. ISSN 1211-412X

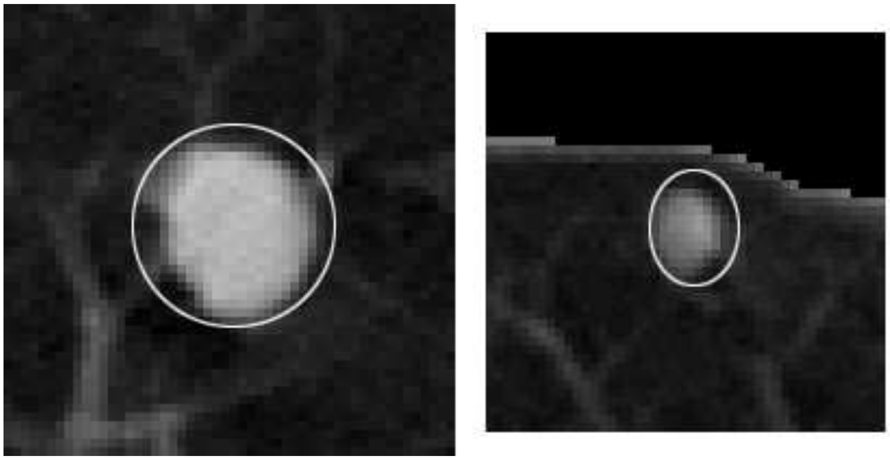

**Figure 7.** Examples of ellipsoids fitted on the nodule.

**Figure 8.** Input slice (left) and non-pleural nodule candidates detected (right) FPs in white , TPs in gray.

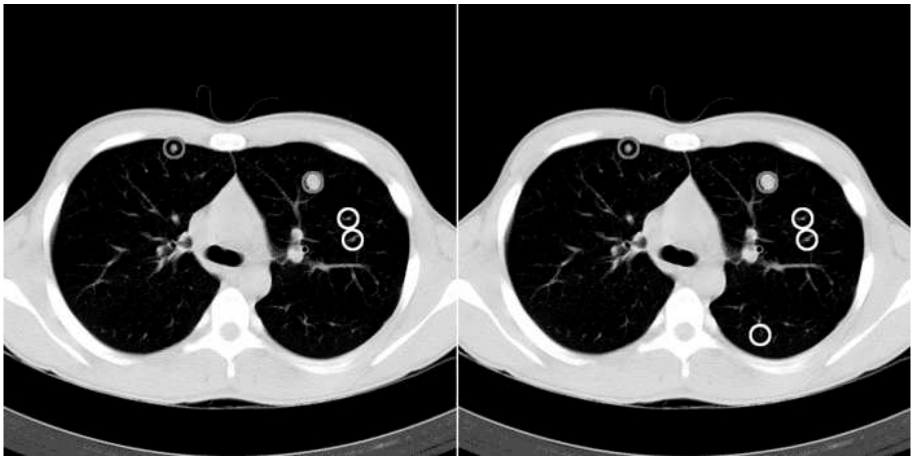

**Figure 9.** Nodules from Figure 8 after classification by FLD based classifier (left) and multi-threshold classifier (right).

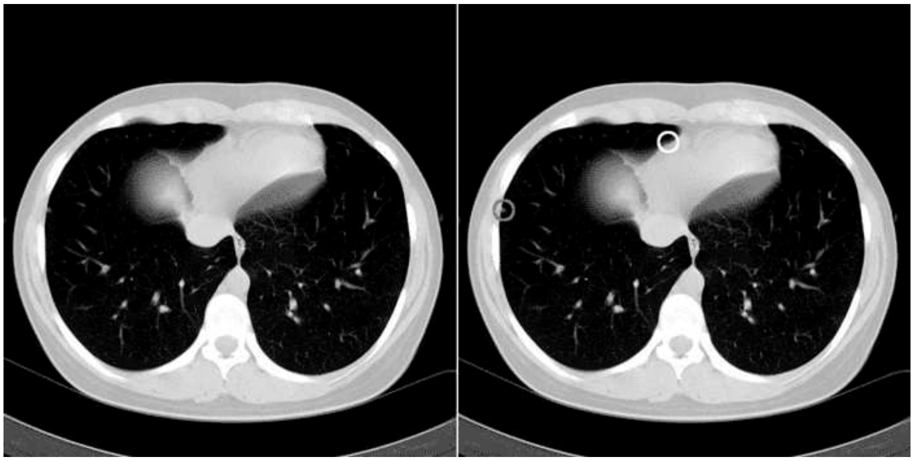

**Figure 10.** Input slice (left) and non-pleural nodule candidates detected (right) FPs in white , TPs in gray.

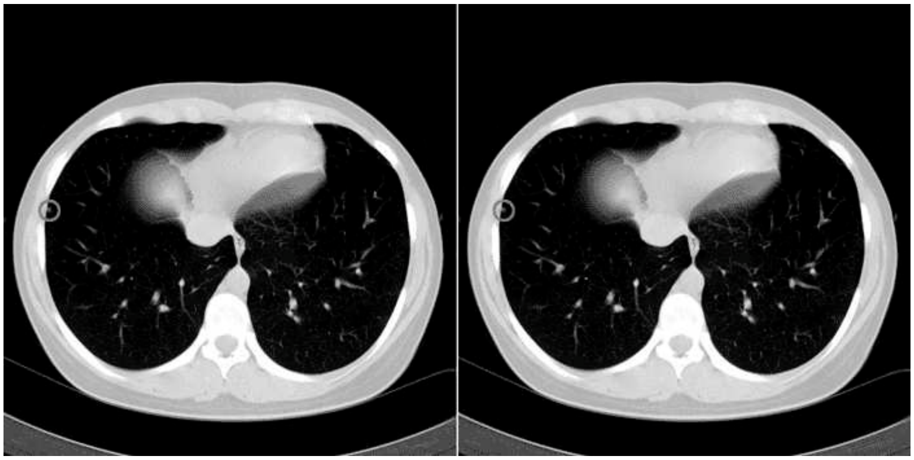

**Figure 11.** Nodules from Figure 10 after classification by FLD based classifier (left) and multi-threshold classifier (right).